

WIND TUNNEL INVESTIGATION OF HELICOPTER LOADS DURING URBAN OPERATIONS ON A BUILDING WITH COLUMNAR VORTEX GENERATORS

J.C. Matías[1], R. Bardera[2], E. Barroso[3], & J. Fernández[4]

[1]National Institute for Aerospace Technology, matiasgjc@inta.es
[2] National Institute for Aerospace Technology, barderar@inta.es
[3] National Institute for Aerospace Technology, barrosobe@inta.es
[4] National Institute for Aerospace Technology, jferant@inta.es

Abstract

The recent development of Urban Air Mobility (UAM) has renewed interest in the complex aerodynamic interactions between aerial vehicles and the urban built environment. One of the most critical challenges is the flow separation generated by the sharp, non-aerodynamic edges of buildings, which creates highly turbulent and non-uniform wakes over rooftops, significantly compromising the safety of helicopter take-off and landing maneuvers. Passive flow control techniques can be employed to mitigate these adverse effects.

Based on previous research conducted by the National Institute for Aerospace Technology (INTA), which demonstrated that Column Vortex Generators (CVG) are capable of significantly reducing flow separation generated by the upwind corner, this study evaluates the impact of these devices on a helicopter operating above the rooftop. Experimental wind tunnel tests were carried out at INTA using 1:70 scaled models of a cube-shaped building and an instrumented helicopter. Aerodynamic forces and moments were acquired using a custom six-component internal balance, supplemented by Particle Image Velocimetry (PIV) and smoke visualizations. The results reveal that the baseline building induces severe load fluctuations, including a sharp 35% increase in the thrust coefficient within the rooftop shear layer. The implementation of CVGs successfully suppresses the recirculation bubble, smoothing the thrust variation to just 15% and reducing rolling moment fluctuations by up to 30%. Crucially, at critical near building operations, the CVGs achieve a 45% reduction in vertical force standard deviation and a 37% to 82% reduction in the multi-component total force deviation. These quantitative findings demonstrate that CVG significantly alleviate pilot workload and enhance operational safety margins, providing vital guidelines for future vertiport infrastructure and architectural design.

Keywords: Urban Air Mobility, Helicopter Aerodynamics, Passive Flow Control, Columnar Vortex Generators, Wind Tunnel Testing

1. Introduction

The ability to hover in close proximity to structures is the most important operational capability making them essential for a wide range of urban missions. These include emergency medical services, surveillance, road traffic control, and rapid transport of personnel in congested metropolitan areas (Figure 1).

In recent years, this operational paradigm has expanded significantly with the develop of Urban Air Mobility and Unmanned Aerial Vehicles (UAVs). Driven by the need to alleviate ground traffic congestion, numerous aerospace companies are designing Personal Air Vehicles (PAVs) [1]. However, establishing the necessary infrastructure for the proper operation of these vehicles presents a complex challenge. Stablish good locations for urban heliports [2] is not an easy task.



Figure 1 – Examples of helicopters operating above building helipads in cities.

Operating a rotary-wing vehicle surrounded by buildings means that the aircraft is inside a hostile aerodynamic environment. Unlike streamlined bodies, urban architectural features behave as bluff bodies with sharp edges. When the atmospheric boundary layer interacts with a building, the incoming flow undergoes massive flow separation, generating large recirculation regions, high velocity gradients, and elevated turbulence intensities. Specifically, when the wind interacts with the upstream facade of a cube-shape building, it creates different flow patterns (Figure 2). A recirculation bubble appears in the lower part, flow acceleration in the upper part and a stagnation point between them. A massive flow separation is created over the roof [3], generating unsteady and sudden changes in air velocity and pressure, and conical vortex [4-6] that degrade the aerodynamic stability of helicopters and UAVs, severely complicating critical take-off and landing maneuvers.

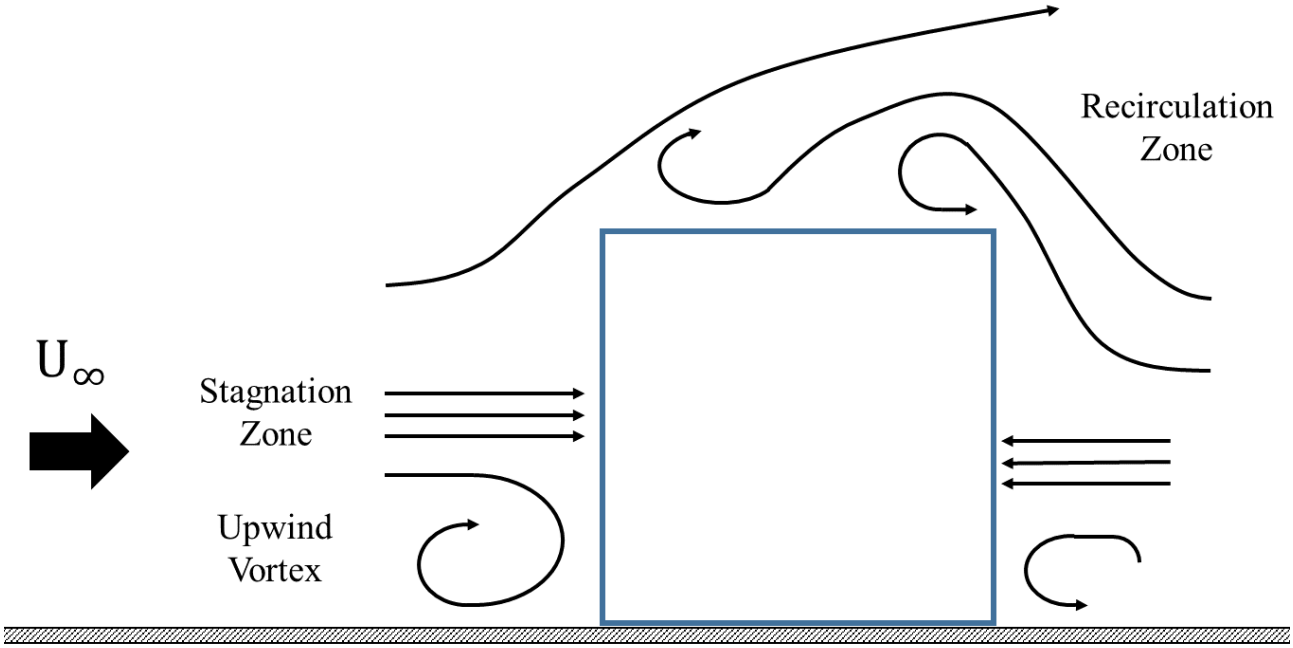


Figure 2 – Flow patterns around a cube-shaped building.

Inside unsteady flows the pilot workload increases substantially, as it requires accurate pilot corrections for controlling the aircraft. It is demonstrated that low frequency oscillations (0.2 to 2 Hz) are the ones that most affect the proper helicopter operation and compromise safety [7,8]. The evaluation of the pilot workload increase can be made through the feedback from real pilots performing landing maneuvers or using high-fidelity helicopter flight simulators [9-15]. The impact of these turbulent airwakes on rotorcraft operations has been extensively documented in maritime environments—such as helicopter-ship dynamic interference on military frigates and aircraft carriers [16-27]. However, despite its critical importance for future cities, with increased number of air

operations and aircrafts, there is a notable gap in the literature regarding the precise aerodynamic loads experienced by a rotatory-wing vehicle operating in the unsteady wake of a building.

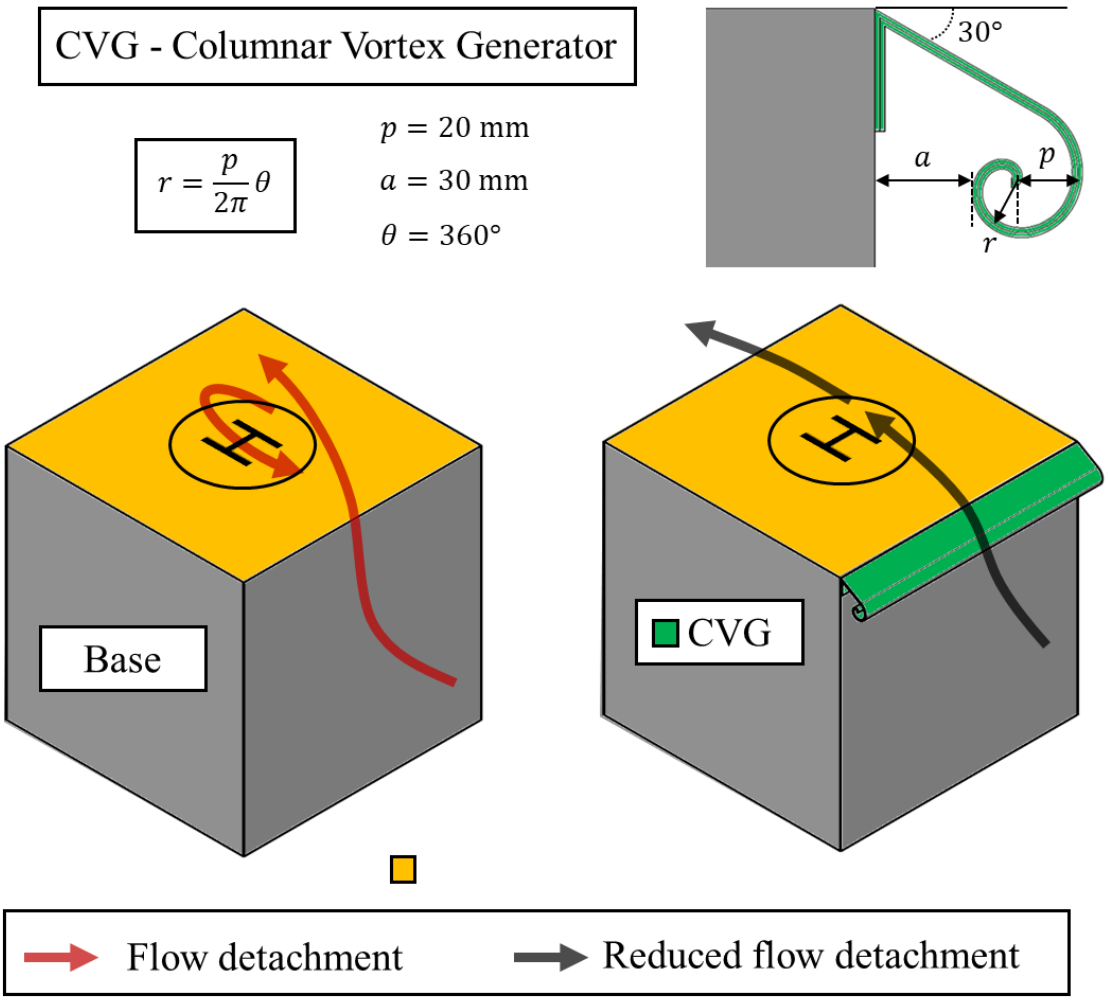


Figure 3 – CVG geometry and aerodynamic changes expected above the helipad at the building rooftop using the CVG.

To mitigate the adverse effects of rooftop flow separation, passive flow control system can be used. For example, a parametric study of different Columnar Vortex Generators (CVGs) was presented with promising results in [28]. Specifically, the CVG30L demonstrated the best reduction of flow detachment generated on the roof, and is the one selected for the present study. The geometry of the CVG is presented in Figure 3 and consist of an arch of Archimedes' spiral and a flat surface at a 30-degree angle to the roof line. The principle of operation of the CVG consist of ingesting tangential flow and discharging axial flow through the sides of the device [29]. In this way, the airflow near the upwind corner of the building can better adapt to the sudden change in geometry and remains attached, thereby preventing or significantly reducing flow separation over the roof where the helicopter operates (Figure 3).

This paper uses smoke and Particle Image Velocimetry (PIV) visualizations, and forces and moments measurements to evaluate how CVG can modify the building wake and how it influences helicopter loads in different heights during landing and take-off maneuvers above the rooftop helipad. The structure of this paper is divided into the following sections. Section 2 will describe the experimental set-up, including the wind tunnel and equipment used for obtaining flow visualizations and helicopter forces determination. Section 3 will present the results of the flow visualizations around the building and aerodynamic forces comparing the base building case with the case with CVG installed.

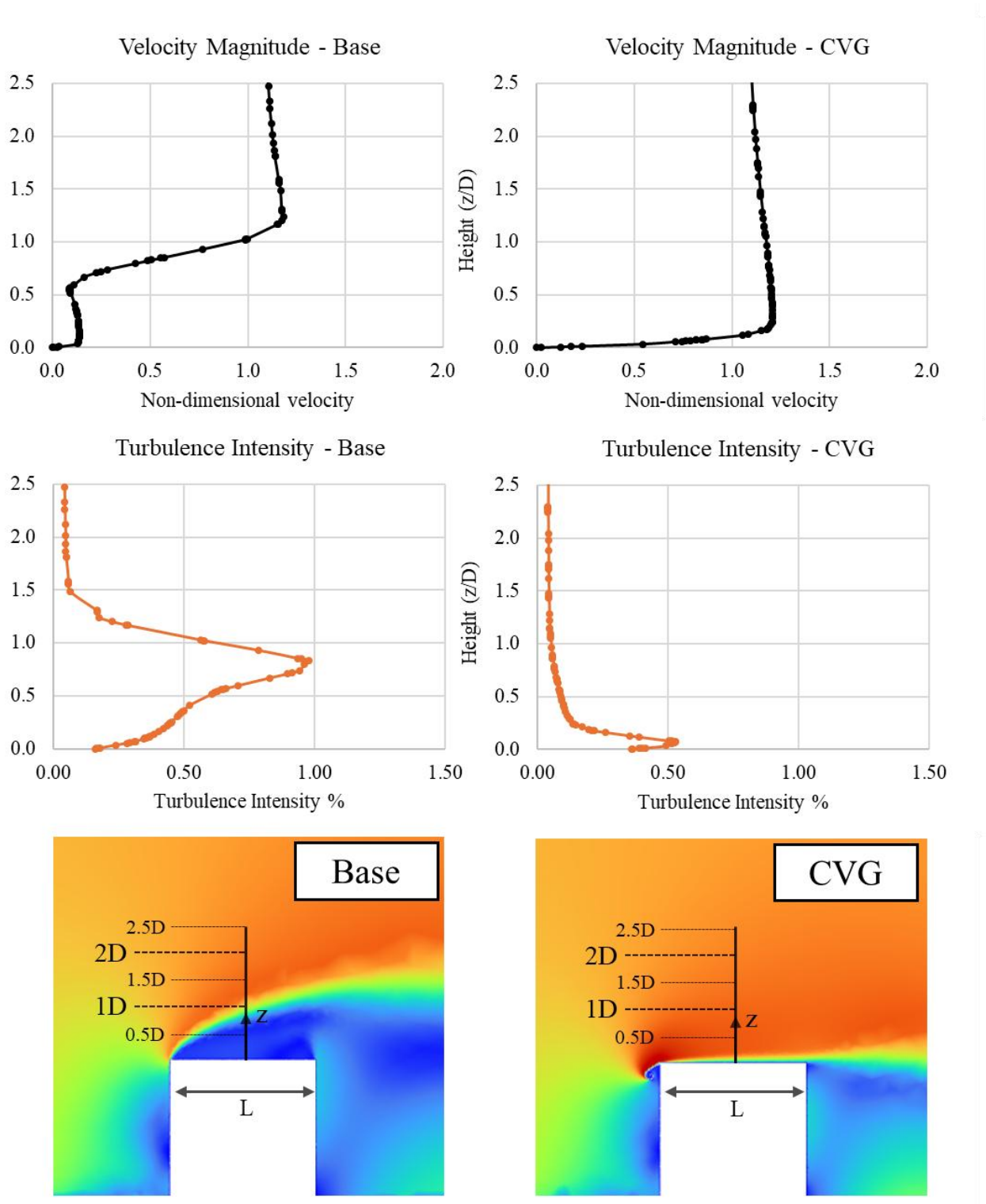


Figure 4 – CFD results for base and CVG building: velocity and turbulence intensity.

1.1 Numerical approach (CFD)

Before obtaining experimental results from wind tunnel tests, a numerical simulation was carried out using CFD to compare the effects on the flow caused by positioning the CVG at the corner of the roof facing the wind. The results of non-dimensional velocity magnitude and turbulence intensity for the base building and the modified using CVG are displayed in Figure 4. Both the non-dimensional velocity contours at the bottom of the Figure 4 and the velocity profiles taken at different heights (dimensionless with respect to the D helicopter rotor) show a significant reduction in the separated flow and the low-velocity region over the roof when the CVG is added. In the case of the base building, velocities predicted above the roof are low (< 50% of the free-stream velocity) for lower

heights 0.8D, and do not reach the free-stream velocity until heights of 1.0D. In the case of CVG, low velocities are only observed in an area very close to the roof (< 0.2D), with velocities up to 30% higher than the free stream flow. The observed turbulence levels show a significant reduction in the areas near the roof when the CVG is added to the building. Thus, the base building exhibits high turbulence values up to heights of 1.2D. However, adding the CVG results in lower turbulence values at much lower heights, meaning that turbulence levels are already very low for helicopter positions above 0.25D. Consequently, the CFD results predict flow velocities much closer to those of free-flow conditions and significantly lower turbulence values, which could lead to improved helicopter control and a reduced pilot workload during the critical maneuver of landing or taking off from the roof of a building.

2. Experimental set-up

2.1 Wind Tunnel and Particle Image Velocimetry (PIV)

The experimental campaign was carried out in the low-speed wind tunnel facility at the National Institute for Aerospace Technology (INTA) in Spain (Figure 5 a). This facility is a closed-circuit wind tunnel featuring an open, elliptical test section with a cross-section of 2 x 3 m^2. Driven by a 420 kW motor operating at maximum power, the tunnel can reach velocities up to 60 m/s, while maintaining a freestream turbulence intensity below 0.5 %. To simulate the ground boundary condition in the vicinity of the building model, an elevated ground-plane platform was installed within the test section. The wind tunnel is fully equipped with aerodynamic force measurement systems and a Particle Image Velocimetry (PIV) system [30–33] to acquire flow visualizations and velocity fields around the models. For the PIV setup (Figure 5 b), the flow was seeded with olive oil tracer particles ~ 1 µm in diameter and illuminated using a dual-cavity, neodymium-doped yttrium aluminum garnet (Nd:YAG) pulsed laser system, capable of delivering a maximum energy output of 190 mJ per pulse. By synchronizing the laser pulses with the acquisition of frame pairs, particle displacements were recorded using a high-resolution digital camera equipped with a 2048 × 2048 pixels Charge-Coupled Device (CCD) sensor. Given the precisely controlled time delay ($\Delta t = 25$ us) between successive frames, a cross-correlation algorithm based on a two-dimensional Fast Fourier Transform (FFT) was utilized to compute the velocity vectors. The processing was performed using interrogation windows of 32 × 32 pixels with a 50 % spatial overlap, in strict compliance with the Nyquist sampling criterion. Throughout the experiments, the camera configuration yielded a field of view of 540 mm. The ensemble-averaged velocity fields presented in this study were derived from 200 instantaneous images and processed into non-dimensional velocity contours using Tecplot 360 software.

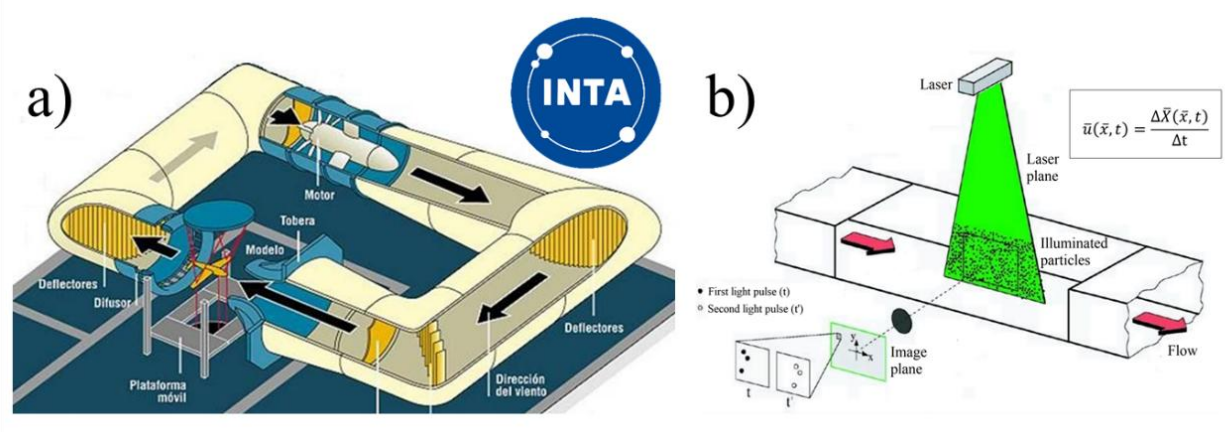


Figure 5 – a) Wind Tunnel T-1 INTA b) Particle Image Velocimetry (PIV) system.

2.2 Building and helicopter scaled models

The building is cube-shaped building model with dimensions of $60 \times 60 \times 60$ cm^3, that corresponds to a $1:70$ scaled version of a real building of 42 m in height with sharp edges. It serves as a representative structure for a rooftop helipad. During the experimental campaign, the model was centered within the wind tunnel test section and resulted in a maximum frontal blockage area of the model of 0.36 m^2, accounting for less than 10% of the wind tunnel cross-sectional area, thereby

mitigating aerodynamic blockage effects. The corresponding Reynolds number based on the building dimmensions was $Re = 2 \times 10^5$, which safely exceeds the critical threshold for sharp-edged bluff bodies ($Re_{crit} > 10^5$), ensuring Reynolds-number-independent flow separation [43]. A photograph of the experimental setup, displaying the scaled building model positioned on the platform, is provided in Figure 6. The building model has been tested using the base geometry and by installing the 3D printed model of the CVG (Columnar Vortex Generator) passive flow controller in the windward corner.

Helicopter scaled model is also presented in Figure 6. The external fuselage geometry of the NH Industries NH-90 helicopter was precisely replicated using high-resolution 3D printing manufacturing techniques. As can be seen in Figure 7, the model houses an internal strain-gauge balance (HELIBAL) to register aerodynamic loads. HELIBAL is a custom six-component internal balance designed and developed at INTA. This instrument measures three orthogonal aerodynamic forces (F_z - thrust, F_y – side force, and F_x – drag) and three aerodynamic moments (M_x - roll, M_y - pitch, and M_z - yaw). The load cell structure is machined from high-strength aluminum and instrumented with strain gauges configured into seven Wheatstone bridges. The mechanical deformations are subsequently converted into aerodynamic forces and moments via a calibrated interaction matrix. A brushless Axi 2204/54 motor drives the five-bladed helicopter main rotor, which features a diameter of $D = 230\ \mathrm{mm}$. The entire scaled rotorcraft assembly is rigidly supported in the wind tunnel by a high-stiffness steel sting bar. This bar is attached to an automated multi-axis positioning system, to place the model in different heights with respect to the building roof during testing.

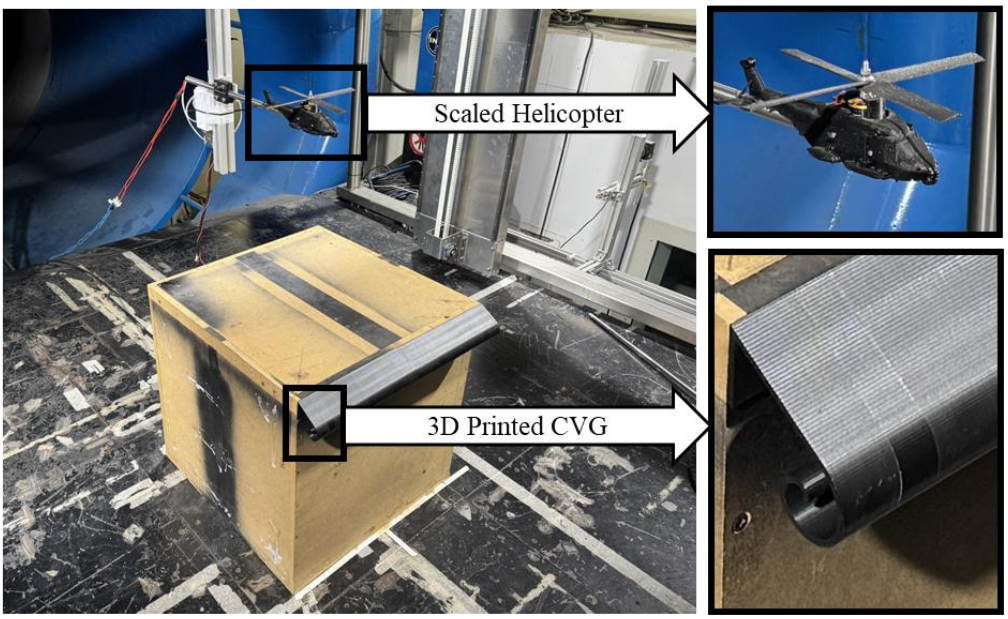


Figure 6 – Building, helicopter and CVG scaled models in wind tunnel test section.

In order to validate the experimental results obtained with the scaled rotorcraft assembly, aerodynamic flow similarity of the main rotor must be established. This similarity is achieved by matching the thrust coefficient (C_T) and the advance ratio (μ) to the full-scale helicopter. The thrust coefficient for the full-scale helicopter under hovering conditions is defined as:

$$C_T = \frac{T_{io}}{\frac{1}{2}\rho A(\Omega \mathrm{R})^2} = 5.70 \times 10^{-3} \tag{1}$$

where T_{io} is the thrust during hovering (equal to helicopter weight, $W = 7\,900\ \mathrm{kg}$), $\rho = 1.225\ \mathrm{kg/m^3}$ is the air density, $A = 208.7\ \mathrm{m^2}$ is the rotor disk area, $\Omega = 270\ \mathrm{rpm}$ is the rotor angular velocity, and

$\mathrm{R} = 8.15\ \mathrm{m}$ is the blade radius.

An equivalent thrust coefficient was matched for the scale model by operating the electric motor at 25 W (10 V and 2.5 A), yielding a scaled rotor speed of $\Omega_s = 4\,350\ \mathrm{rpm}$ rpm and a measured model thrust coefficient of $C_T = 5.70 \times 10^{-3}$ via the HELIBAL balance.

Furthermore, kinematic similarity was maintained by matching the advance ratio (μ). The simulated operational wind speed condition corresponds to $U_\infty = 20\ \mathrm{m/s}$. Given that the angular velocities of the full-scale and scaled helicopters are known ($\Omega = 300\ \mathrm{rpm}$, $\Omega_s = 4{,}350\ \mathrm{rpm}$) along with their respective rotor radius ($R = 8.15\ \mathrm{m}$, and $R_s = 0.11\ \mathrm{m}$), the advance ratio (μ) similarity condition is governed by:

$$\mu = \frac{U_\infty}{\Omega \mathrm{R}} = \frac{V_{tunel}}{\Omega_s \mathrm{R_s}} \tag{2}$$

Consequently, this similarity criteria yields a target wind tunnel freestream velocity of $V_{tunnel} = 4.50\ \mathrm{m/s}$ to achieve full kinematic similitude during the tests.

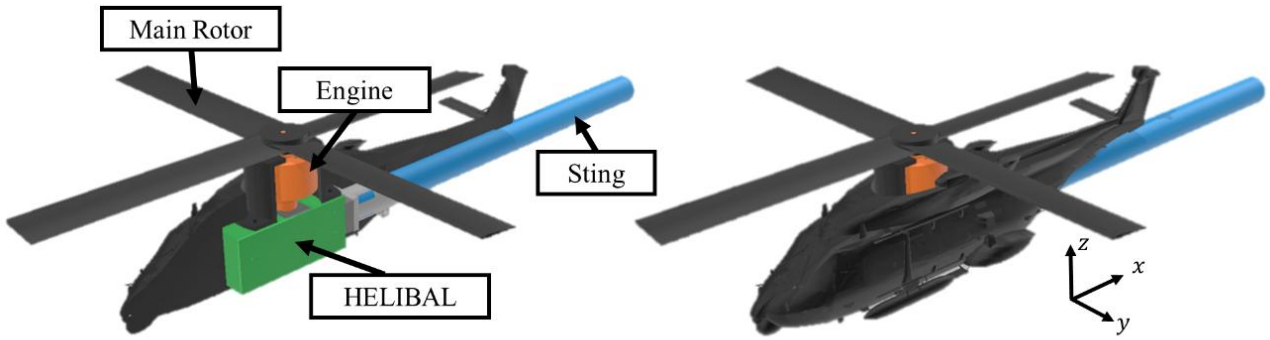


Figure 7 – Full assembly of the helicopter model.

3. Results

This section will show the flow visualisations and the average aerodynamic forces and moments of the helicopter in various positions above the building helipad on the roof. The helicopter will always be positioned at the centre of the roof, at various heights above the platform, as shown in Figure 8. The heights will always be non-dimensional, relative to the diameter of the helicopter's main rotor ($D = 230\ \mathrm{mm}$).

3.1 Flow visualization: smoke and Particle Image Velocimetry (PIV) tests

The smoke visualisation tests are shown in Figure 9. During the rooftop landing manoeuvre, when the helicopter is still at a height greater than one diameter (1.0D), it is still operating in an area outside the region of separated flow and low velocities generated by the base building. As it descends, when the helicopter is at a height of 0.6 diameters, the helicopter is already completely immersed in the bubble zone generated by the roof. In the case with the CVG, the smoke clearly shows that the flow does not generate such a large separation at the upwind corner and the helicopter is still hovering in a clean-flow zone. Finally, before contact (height 0.4D), the smoke shows that the helicopter is in the lower part of the flow recirculation zone and, with the CVG installed, the flow follows the actuator and moves parallel to the roof, striking the fuselage and rotor directly, with no low-speed zones presence.

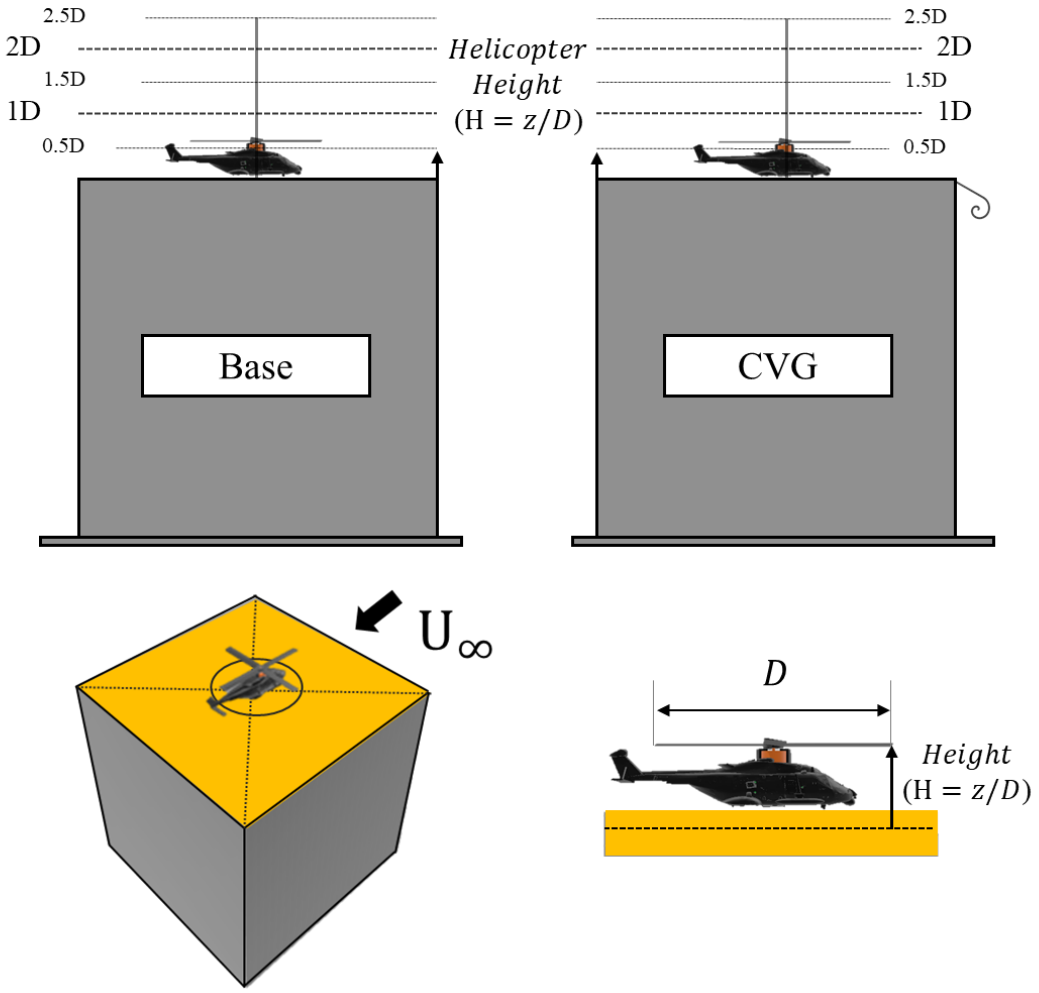


Figure 8 – Helicopter positions above the roof with height in rotor diameters (D).

The same effect observed in the smoke can be seen in the dimensionless velocity contours obtained using PIV, shown in Figure 10. These figures show the flow over the roof and near the upwind corner, with and without CVG installed (Base). In the first cases without a helicopter (Base and CVG), a significant difference can be seen between the flow patterns generated by the wind detachment on the windward corner. The base case reveals that the flow detaches and go upwards generating a big recirculation area above the roof.

This low-speed area is very different from the flow outside the building's area of influence and may interfere with the proper operation of aircrafts on the rooftop helipad. This entire region of detached flow is corrected by adding the CVG device. In this case, the airflow accelerates and, with almost no separation, continues parallel to the roof surface. So the helicopter can experience airflow that is much more similar to the external airflow, without encountering high gradients in the incident velocity during take-off or landing. To get a better idea of how the aerodynamics of the helicopter interfere in both situations, PIV velocity contours were obtained with the helicopter operating at different heights, from 0.4 to 1.2 diameters. Only two representative cases are shown to illustrate how the flow changes when the effect of the main rotor blades is introduced into the aerodynamic problem: 0.4D and 0.8D.

In the first case, when the helicopter is flying at low altitude (0.4D), the base case shows that the rotor operates in the aforementioned low-speed region, accelerating the velocities of the recirculation bubble generated by the wake separation at the upwind corner. The effect of operating the helicopter alongside the CVG at low altitude is shown in the velocity contour next to it (CVG + H0.4D). It is clear

that although a small region of separation and recirculation appears, this affects the fuselage, but the rotor is in a flow zone with velocities similar to those in free flow (1.0 and up to 1.2 in dimensionless terms).

The final case shown corresponds to the helicopter at a height of 0.8 diameters. In the base case, the helicopter continues to interact with the flow detached by the corner of the building, causing its rotor to operate in a shear zone, which separates the low- and high-speed flows away from the building. This can subject the helicopter to significant vibrations, which are difficult for the pilot to control in a situation that is critical, given the proximity of the building. In the case of the CVG, with the helicopter at the same height, the velocity contour shows that the rotor is not affected by the flow patterns generated by the building; consequently, vibrations and undesirable phenomena could be reduced, as the helicopter is operating in a flow that is virtually unaffected by the building's presence.

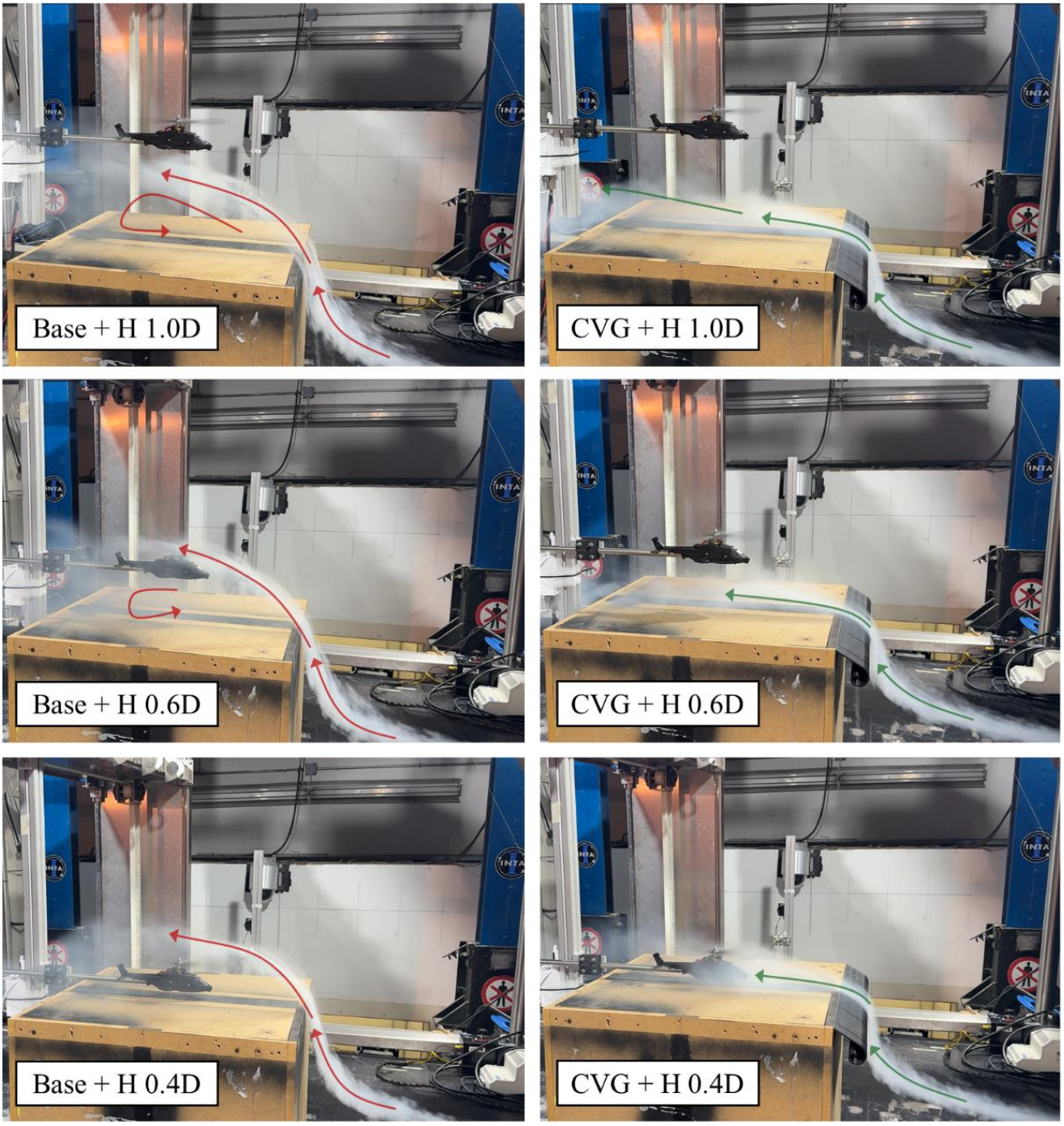


Figure 9 – Smoke visualization above the rooftop for base and CVG with helicopter.

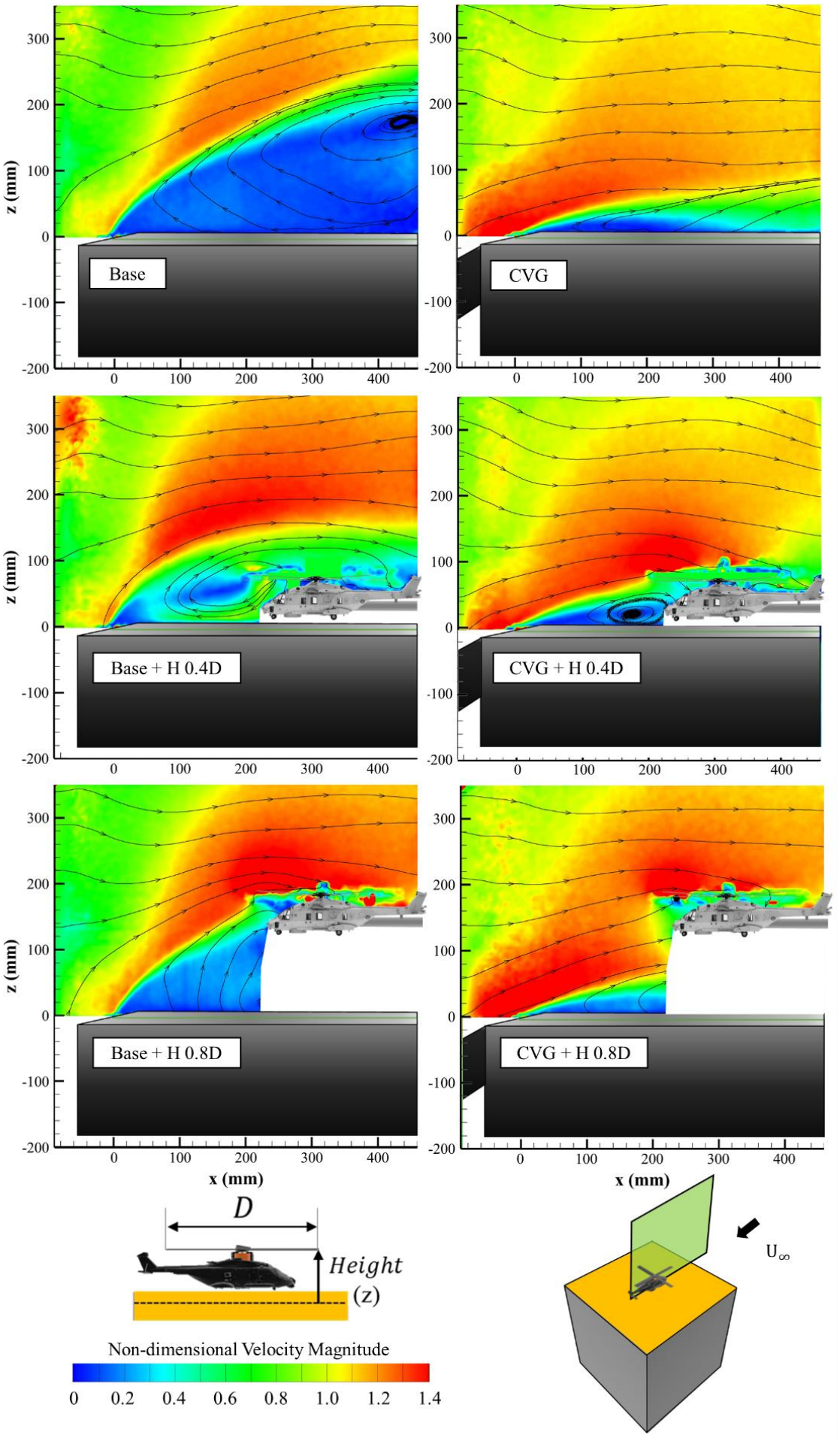


Figure 10 – PIV non-dimensional velocity contours above the rooftop for base and CVG.

3.2 Mean aerodynamic forces and moments

Following the visualisation tests, the helicopter's aerodynamic forces and moments were recorded at different heights above the center of the rooftop helipad platform. Specifically, the helicopter was simulated in a hovering flight and always facing to the upcoming wind direction at 20 different heights ranging from 0.4D to 2.2D to obtain the results shown in Figure 11. Vertical axis displays the helicopter height in rotor diameters (z/D), and horizontal axis shows forces and moments presented in non-dimensional terms as,

$$C_{Fi} = \frac{F_i}{\frac{1}{2}\rho A(\Omega \mathrm{R})^2} \qquad C_{Mi} = \frac{M_i}{\frac{1}{2}\rho A(\Omega \mathrm{R})^2 R} \tag{3}$$

where $i = x, y, z$ corresponds to the different components measured, ρ is the air density, Ω is the angular speed, R is the main helicopter rotor radius and S is the rotor surface.

The first two graphs in Figure 11 display the thrust (C_{Fz}) and longitudinal (C_{Fx}) force coefficients for the base and CVG case. Lateral force coefficient (C_{Fy}) is not displayed since the helicopter is on the center and lateral forces are null. The longitudinal force coefficient undergoes minor changes along the helicopter's flight path over the roof at different heights. It should be noted, however, that in the base case, the low speeds of the recirculation bubble result in negative values below 1.5D. Above that height, the values are practically zero. When we add the CVG to the building, the values remain small, but they are always positive due to the elimination of flow recirculation and the effect of headwind on the helicopter. The thrust coefficient (C_{Fz}) does vary significantly. Specifically, in the base model, the coefficient increases sharply by up to 35% between low heights (0.5D) and heights where it is affected by the shear layer of the flow detachment (0.8D–1.4D). This increase in the drag coefficient can cause vibrations and sudden changes in flight conditions that compromise maneuver stability.

Once the helicopter exceeds a height of 1.5D, neither the ground effect nor the flow separation zone affects it, so the drag coefficient returns to uniform values of around $C_{Fz} = 1 \times 10^{-2}$. This sudden increase in thrust is corrected by the CVG device. Between 0.4D and 2.0D, variations in thrust occur, but these are much smoother and more uniform than in the base case. Specifically, maximum variations of 15% can be observed between 0.4D and 1.0D.

The graphs in the middle of Figure 11 show the values of pitch (C_{My}) and rolling (C_{Mx}) coefficients. The rolling moment for the base building case shows significant fluctuation at low heights (between 0.4D and 1.4D), peaking at 0.9D, representing a maximum difference in the coefficient of up to 1.0E-04. The same coefficient measured with the CVG installed in the building reveals a reduction in variations of up to 30% with respect to the base case, presenting much more uniform values and eliminating the peak at low heights. Greater differences can be observed for the pitch coefficient, where the base case shows a sharp variation in the coefficient of 3.3E-04 between low heights (0.5D) and high heights (>1.5D). Once again, the CVG corrects this trend, with C_{My} values showing an increase of 1.1E-04 between 0.4D and 1.5D and a further progressive increase of up to 1.5E-04 between 1.5D and 2.2D. In this way, adding the CVG reduces total fluctuations by up to 20%, and the changes occur much more gradually and safely for helicopter operation.

Finally, the two graphs at the bottom of Figure 11 show the standard deviation of the force coefficients recorded during the 30-second acquisition period at each point for the three axes ($STD\ C_{Fx}, C_{Fy}, C_{Fz}$). Although fluctuations in lateral (σ_{F_y}) and longitudinal (σ_{F_x}) forces do not differ significantly between the base case and the CVG, the thrust force (σ_{F_z}) shows significant changes, especially at low altitudes, which is where adding CVG has the greatest effect. At these low heights relative to the building roof (< 1.0D), the deviations in the vertical force are up to 3.5E-04 for the base case and only 1.9E-04 for the case with CVG, representing a 45% reduction. These fluctuations can

be directly linked to the pilot's workload during take-off or landing maneuvers over the building; therefore, halving their value could significantly reduce workload and enhance operational safety.

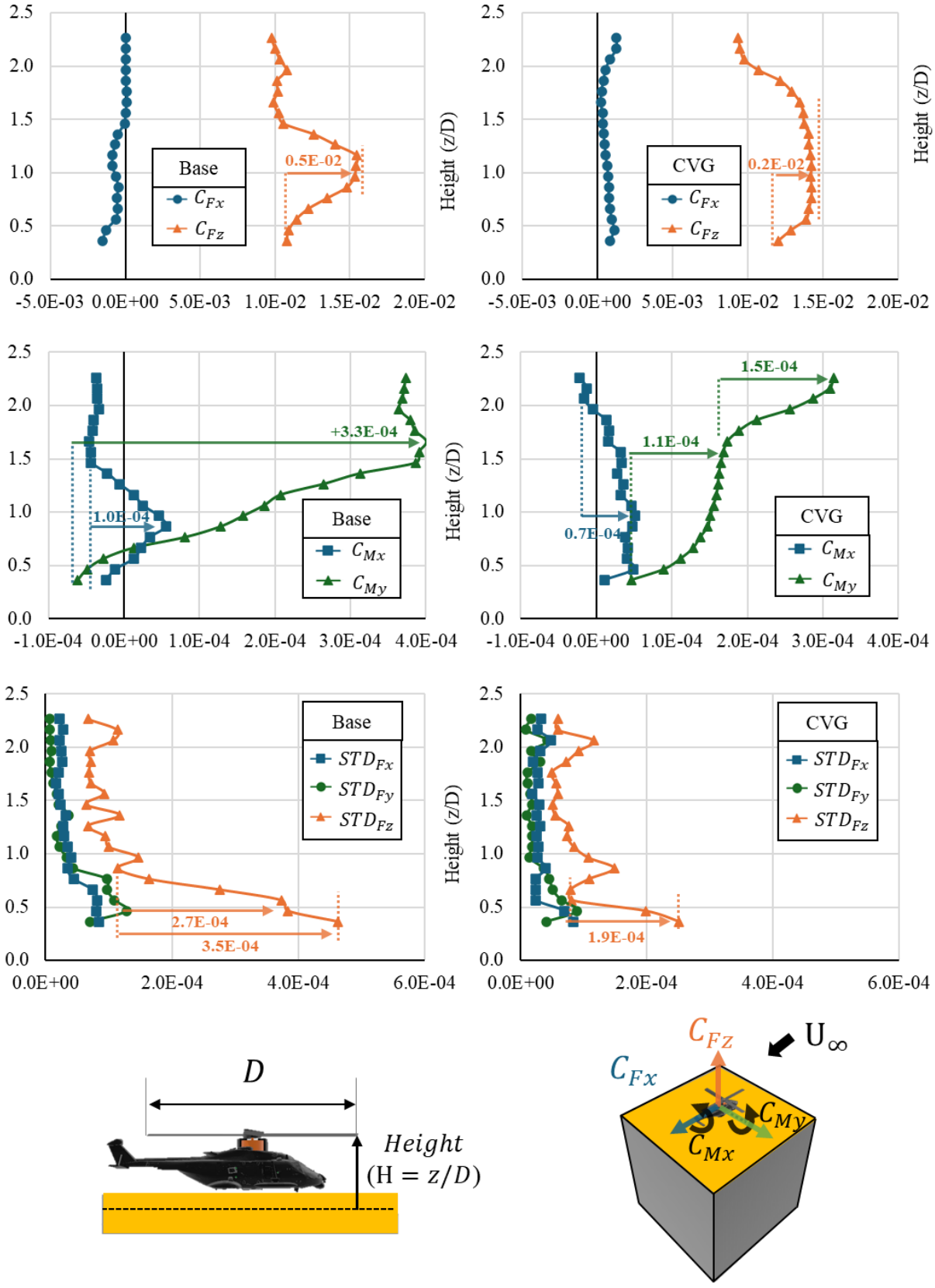


Figure 11 – Mean forces and moments of the helicopter hovering with and without CVG.

Figure 12 shows the result of combining the deviations of the measured forces in the three components into a single one, using the following expression,

$$\% \, STD = \left(\frac{\sqrt{C_{Fx}^2 \sigma_{Fx}^2 + C_{Fy}^2 \sigma_{Fy}^2 + C_{Fz}^2 \sigma_{Fz}^2}}{C_{Fx}^2 + C_{Fy}^2 + C_{Fz}^2} \right) \times 100 \quad (4)$$

In this way, this value is computed for each dimensionless altitude (between 0.4D and 2.3D) and for the base case and the case with the CVG installed in the building. The results show, in general, a significant reduction in force deviations. With the exception of heights of 0.9D, 1.3D, and 2.0D, the remaining cases show significantly lower deviations for the CVG case. Particularly important are the cases at low altitude above the building (< 0.9D), where the reduction in deviations as a percentage ranges from 37% to 82% for the CVG case. These are precisely the most critical points of the operation given the helicopter's proximity to the building.

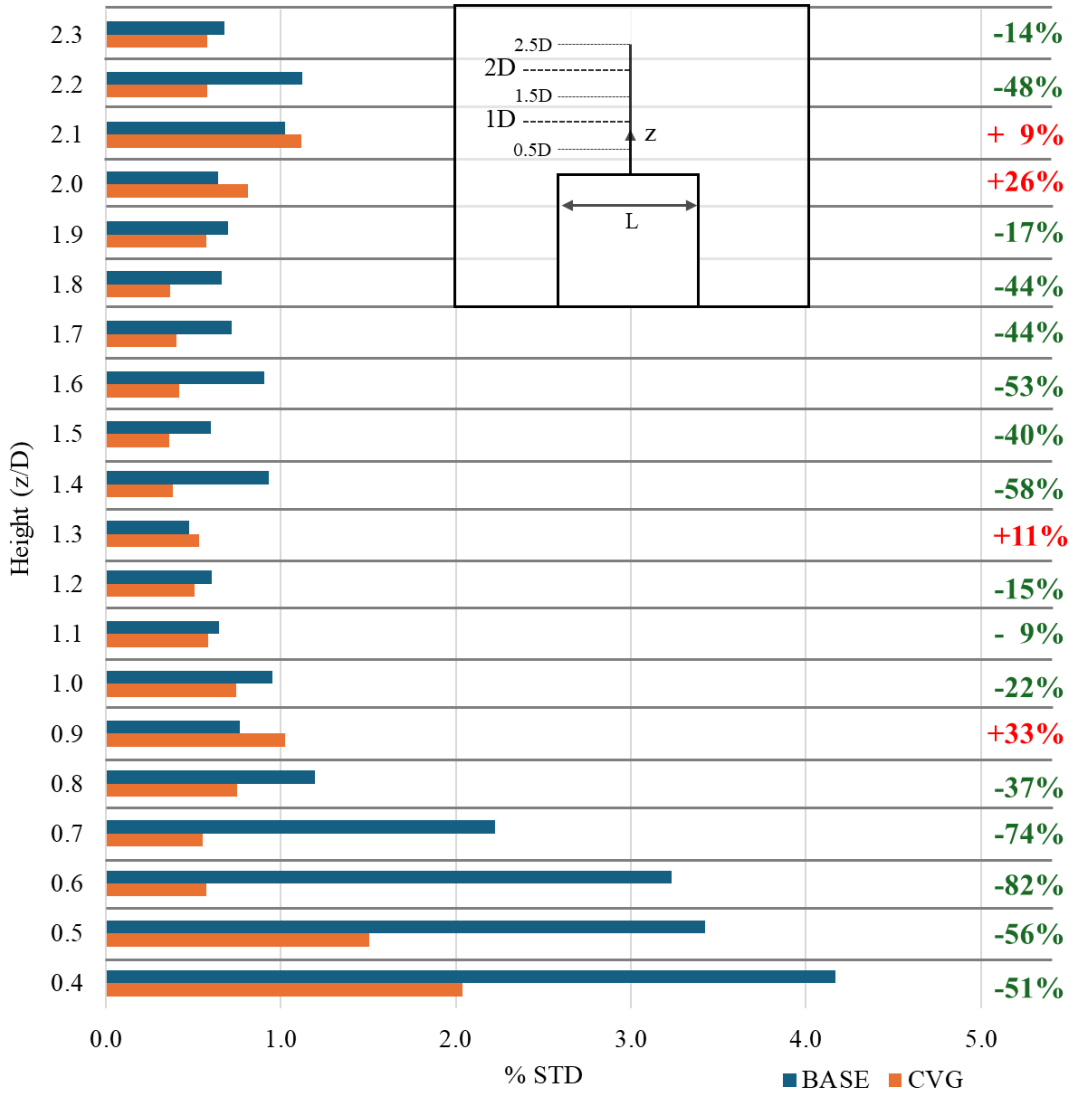


Figure 12 – Standard deviation of forces measured at different helicopter heights for base and CVG.

4. Conclusions

This paper presented a comprehensive wind tunnel investigation evaluating the aerodynamic interference and load variations experienced by a scaled helicopter model during urban operations atop a cube-shaped building, contrasting a baseline architectural configuration against one equipped with Columnar Vortex Generators (CVGs) as a passive flow control system. The integration of qualitative smoke visualizations, quantitative Particle Image Velocimetry (PIV), and six-component internal balance measurements of the helicopter confirmed the aerodynamic wake mitigation above

the roof, the stabilization of aerodynamic coefficients and the reduction in pilot workload and operational safety of the helicopter.

Smoke visualizations and PIV velocity fields confirmed that the baseline building induces massive flow separation at the sharp windward roof corner, creating a severe low-velocity recirculation bubble that encapsulates the helipad zone up to a height of 1.5D. The implementation of CVG effectively corrects this detached flow region by accelerating the incoming airflow and forcing it to remain parallel to the rooftop surface. Consequently, the rotorcraft encounters a significantly more uniform and clean velocity field, suppressing severe velocity gradients during the critical landing and take-off phases. From the point of view of rotor-wake interaction, at low operational altitudes 0.4D, the baseline rotor interacts directly with the highly unsteady separation bubble, accelerating the low-speed recirculation structures. Conversely, with the CVGs installed, the main rotor operates in a flow zone with freestream-like non-dimensional velocities (1.0 to 1.2). At intermediate heights (0.8D), the baseline rotor is subjected to a severe shear layer separating low and high-speed flow regions, which can produce adverse structural vibrations for the helicopter. The CVGs entirely eliminate this interaction, ensuring the rotor remains virtually unaffected by the building's aerodynamic wake.

Force and moment measurements revealed that the baseline configuration induces abrupt aerodynamic load variations along the helicopter's descent path. Most notably, the baseline thrust coefficient (C_{Fz}) exhibits a sharp increase of up to 35% between 0.5D and 1.4D due to shear layer interaction, threatening flight stability. The CVGs successfully smooth this trend, bounding the maximum thrust variation to just 15% across the entire operational procedure (0.4D to 2.0D). Furthermore, the installation of CVG reduces total fluctuations in the rolling moment by up to 30% at low altitudes and dampens pitch coefficient (C_{My}) fluctuations by 20%, ensuring a more gradual and predictable control response for the aircraft.

The unsteady fluctuations of the aerodynamic loads, quantified via standard deviations during the acquisition period, serve as a direct indicator of pilot workload. While longitudinal and lateral force fluctuations remained comparable, the thrust force standard deviation (σ_{Fz}) within the critical near-roof region (< 1.0D) was reduced by 45%. Ultimately, the combined multi-component force deviation metric (% STD) displayed that under low operational altitudes (< 0.9D), where the proximity to the structure maximizes risk, the installation of CVG achieves a remarkable 37% to 82% reduction in total force deviations.

In summary, the experimental evidence demonstrates that Columnar Vortex Generators constitute a highly effective, passive aerodynamic device for urban infrastructure. By significantly mitigating the structural airwake, smoothing mean aerodynamic loads, and drastically reducing unsteadiness at low altitudes. CVG could substantially alleviate pilot workload and enhance the safety margins for helicopter and future Urban Air Mobility (UAM) operations in dense metropolitan environments.

5. Contact Author Email Address

mailto: matiasgjc@inta.es

6. Copyright Statement

The authors confirm that they, and/or their company or organization, hold copyright on all of the original material included in this paper. The authors also confirm that they have obtained permission, from the copyright holder of any third party material included in this paper, to publish it as part of their paper. The authors confirm that they give permission, or have obtained permission from the copyright holder of this paper, for the publication and distribution of this paper as part of the ICAS proceedings or as individual off-prints from the proceedings.

References

[1] Lewe J-H, Briceno S, Schrage D and Mavris DN. An integrated decision-making method to identify design requirements through agent-based simulation for personal air vehicle system. *AIAA Aircraft Technology, Integration, and Operations (ATIO) 2002 Technical Forum*, Los Angeles, CA, 1-3 October 2002, AIAA Paper 2002-5849.

[2] McKinley JB. *Evaluating wind flow around buildings on heliport placement*. Technical Report DOT/FAA/PM-84/25, Defense Technical Information Center, USA, 1984.

[3] *ASHRAE Handbook: Fundamentals (SI Edition)*. Atlanta: ASHRAE Inc., 2005, pp. 31-47.

[4] Cai J, Tsai H-M, Luo S and Liu F. Vortex core and its effects on the stability of vortex flow over slender conical bodies. *AIAA Journal* 2003; 41(11): 2104–2112. doi: 10.2514/2.6834

[5] Banks D and Meroney RN. A model of roof-top surfaces pressures produced by conical vortices: Evaluation and implications. *Journal of Wind Engineering and Industrial Aerodynamics* 2001; 89(6): 477-498. doi: 10.1016/S0167-6105(00)00076-7

[6] Franchini S, Pindado S, Meseguer J and Sanz-Andrés A. A parametric, experimental analysis of conical vortices on curved roofs of low-rise buildings. *Journal of Wind Engineering and Industrial Aerodynamics* 2005; 93(8): 639-650. doi: 10.1016/j.jweia.2005.06.004

[7] Lee R and Zan S. Wind tunnel testing of a helicopter fuselage and rotor in a ship airwake. *Journal of the American Helicopter Society* 2005; 50(4): 326-337. doi: 10.4050/JAHS.50.326

[8] Lee RG and Zan SJ. Unsteady aerodynamic loading on a helicopter fuselage in a ship airwake. *Journal of the American Helicopter Society* 2004; 49(2): 149–159. doi: 10.4050/jahs.49.149

[9] Thedin R, Kinzel MP, Horn JF and Schmitz S. Coupled simulations of atmospheric turbulence-modified ship airwakes and helicopter flight dynamics. *Journal of Aircraft* 2019; 56(2): 812–824. doi: 10.2514/1.C035158

[10] Memon WA, Owen I and White MD. Motion fidelity requirements for helicopter-ship operations in maritime rotorcraft flight simulators. *Journal of Aircraft* 2019; 56(6): 2189–2209. doi: 10.2514/1.C035521

[11] Watson NA, Owen I and White MD. Piloted flight simulation of helicopter recovery to the Queen Elizabeth class aircraft carrier. *Journal of Aircraft* 2020; 57(4): 742–760. doi: 10.2514/1.C035733

[12] Forrest J, Kaaria C and Owen I. Evaluating ship superstructure aerodynamics for maritime helicopter operations through CFD and flight simulation. *The Aeronautical Journal* 2016; 120(1232): 1578–1603. doi: 10.1017/aer.2016.76

[13] Forsythe J, Lynch E, Polsky S and Spalart P. Coupled flight simulator and CFD calculations of ship airwake using Kestrel. In: *53rd AIAA Aerospace Sciences Meeting*, Kissimmee, FL, 5-9 January 2015, AIAA Paper 2015-0556. doi: 10.2514/6.2015-0556

[14] Foeken M and Pavel MD. *Investigation on the simulation of helicopter/ship operations*. Technical Report, Faculty of Aerospace Engineering, Delft University of Technology, The Netherlands, 2005.

[15] Mehling T, Halbe O, Gasparac T, Vrdoljak M and Hajek M. Piloted simulation of helicopter shipboard recovery with visual and control augmentation. In: *AIAA Scitech 2021 Forum*, Virtual Event, 11-15 & 19-21 January 2021, AIAA Paper 2021-1136. doi: 10.2514/6.2021-1136

[16] Chen CH, Wang Y, White MD and Owen I. An experimental technique for evaluating the aerodynamic impact of ship superstructures on helicopter operations. *Ocean Engineering* 2013; 61: 97–108. doi: 10.1016/j.oceaneng.2012.12.052

[17] Bardera-Mora R, León Calero M and García-Magariño A. Aerodynamic effect of the aircraft carrier island on flight deck flow with cross wind. *Proceedings of the Institution of Mechanical Engineers, Part M: Journal of Engineering for the Maritime Environment* 2018; 232(2): 145–154. doi: 10.1177/1475090216689172

[18] Healey JV. Establishing a database for flight in the wakes of structures. *Journal of Aircraft* 1992; 29(4): 559–564. doi: 10.2514/3.46213

[19] Dooley GM, Krebill AF, Martin JE, Buchholz JHJ and Carrica PM. Structure of a ship airwake at multiple scales. *AIAA Journal* 2020; 58(5): 2005–2013. doi: 10.2514/1.J058994

[20] Thedin R, Murman S, Horn J and Schmitz S. Effects of atmospheric turbulence unsteadiness on ship airwakes and helicopter dynamics. *Journal of Aircraft* 2020; 57(3): 534–546. doi: 10.2514/1.C035643

[21] Yuan W, Wall A and Lee R. Combined numerical and experimental simulations of unsteady ship airwakes. *Computers & Fluids* 2018; 172: 29-53. doi: 10.1016/j.compfluid.2018.06.012

[22] Crozon C, Steijl R and Barakos GN. Numerical study of helicopter rotors in a ship airwake. *Journal of Aircraft* 2014; 51(6): 1813–1832. doi: 10.2514/1.C032535

[23] Brownell C, Luznik L, Snyder M, Kang H and Wilkinson C. In situ velocity measurements in the near-wake of a ship superstructure. *Journal of Aircraft* 2012; 49(5): 1440-1450. doi: 10.2514/1.C031668

[24] Bardera R. Flow field velocity on the flight deck of a frigate. *Proceedings of the Institution of Mechanical Engineers, Part G: Journal of Aerospace Engineering* 2014; 228(14): 2674–2680. doi: 10.1177/0954410014524183

[25] Bardera-Mora R, Barcala-Montejano M, Rodríguez-Sevillano A, de Diego G and de Sotto M. A spectral analysis of laser Doppler anemometry turbulent flow measurements in a ship air wake. *Proceedings of*

the Institution of Mechanical Engineers, Part G: Journal of Aerospace Engineering 2015; 229(12): 2309-2320. doi: 10.1177/0954410015573425

[26]Van Muijden J, Boelens O, van der Vorst J and Gooden J. Computational ship airwake determination to support helicopter-ship dynamic interface assessment. In: *21st AIAA Computational Fluid Dynamics Conference*, San Diego, CA, 24-27 June 2013, AIAA Paper 2013-3078. doi: 10.2514/6.2013-3078

[27]Wakefield NH, Newman SJ and Wilson PA. Helicopter flight around a ship's superstructure. *Proceedings of the Institution of Mechanical Engineers, Part G: Journal of Aerospace Engineering* 2002; 216(1): 13–28. doi: 10.1243/0954410021533391

[28] Bardera R, Barcala-Montejano MA, Rodriguez-Sevillano A, León-Calero M and Matías-García JC. Passive flow control over the roof of buildings by using columnar vortex generator. *International Journal of Civil Engineering and Construction Science* 2018; 5(2): 32-42.

[29]Bardera R and Matías García JC. Model of the flow on columnar vortex generator. *Fluid Dynamics Research* 2020; 52(2): 025502. doi: 10.1088/1873-7005/ab5c32

[30]Raffel M, Willert CE, Scarano F, Kähler CJ, Wereley ST and Kompenhans J. *Particle image velocimetry: A practical guide*. 3rd ed. Cham: Springer International Publishing, 2018.

[31]Adrian RJ and Westerweel J. *Particle image velocimetry*. Cambridge: Cambridge University Press, 2011.

[32]Prasad AK. Particle image velocimetry. *Current Science* 2000; 79(1): 51-60.

[33]Adrian RJ. Particle-imaging techniques for experimental fluid mechanics. *Annual Review of Fluid Mechanics* 1991; 23(1): 261–304. doi: 10.1146/annurev.fl.23.010191.001401